



Shahrood University of  
Technology



Iranian Society of  
Mining Engineering  
(IRSM)

# Mapping Lithological Units of an Evaporite Formation using ASTER data: a Case Study from Zagros Fold Belt, SW Iran

Khadijeh Validabadi Bozcheloei\*, and Majid Hashemi Tangestani

Faculty of Geoscience, Shiraz university, Shiraz, Iran

## Article Info

Received 20 September 2023

Received in Revised form 6  
November 2023

Accepted 12 November 2023

Published online 12 November  
2023

DOI: [10.22044/jme.2023.13629.2518](https://doi.org/10.22044/jme.2023.13629.2518)

## Keywords

ASTER

Evaporite

Principal component analysis

Band ratio

## Abstract

Evaporites are sediments that chemically precipitate due to the evaporation of an aqueous solution. Most evaporite formations, in addition to evaporite minerals, include detrital rocks such as mudstone, marl, and siltstone. Principal Component Analysis (PCA), Directed Principal Component Analysis (DPCA), and Band Ratio methods were applied to Advanced Space-borne Thermal Emission and Reflection Radiometer (ASTER) data for mapping the Gachsaran evaporite formation and distinguishing its lithological units in the Masjed Soleiman oil field, located in southwestern Iran. This oil field was the first recognized oil field in the Middle East. Colour composites of PCs 4, 5, and 2, as RGB images, effectively discriminated this formation from other sedimentary formations. The gypsum spectrum, resampled to the 9 band centres of ASTER, exhibited reflectance in bands 4 and 8 and absorption in bands 6 and 9. As a result, these bands were selected for DPCA application. PC4 effectively highlighted gypsum outcrops as bright pixels, while the band ratio 2/1 accentuated ferric iron, appearing as bright pixels, which correlated with the red marls. The results of this study demonstrate that ASTER image processing is a cost- and time-effective method that can be utilized for mapping evaporite formations and distinguishing their lithological units.

## 1. Introduction

Geological maps are traditionally generated through conventional ground surveys, relying on field observations that may inevitably introduce errors, leading to inaccuracies. In the recent decades, optical remote sensing within the visible and near-infrared wavelengths has emerged as a rapid and cost-effective method for gathering valuable information regarding the mineralogical and chemical compositions of outcrops. This advancement offers opportunities to create new lithological maps in regions, where geological mapping is lacking and to enhance the precision of existing ones.

The utilization of satellite image processing for this purpose has gained momentum since the launch of Landsat-1 in 1972. Numerous studies have underscored the efficacy of remote sensing techniques in

extracting geological information, particularly in remote or inaccessible areas. The Advanced Space-borne Thermal Emission and Reflection Radiometer (ASTER), onboard on the TERRA platform launched in December 1999, stands out as a valuable super-spectral imaging system for geological mapping.

ASTER data have been extensively employed in regional mapping to delineate various lithological units including granites, ophiolite sequences, and basement rocks [1, 2, 3, 4]. In this study, we leverage ASTER data to map an evaporite formation and distinguish its lithological components.

Evaporites are sedimentary rocks that form through chemical precipitation resulting from the evaporation of limited surface water on Earth. The most common minerals found in evaporites are halite, anhydrite, and

✉ Corresponding author: [Khvalid@gmail.com](mailto:Khvalid@gmail.com) (K. Validabadi Bozcheloei)

gypsum. These sedimentary deposits have garnered significant attention in geological studies due to their capacity to preserve information about the geological and environmental conditions during their deposition. Furthermore, evaporites serve as highly effective cap rocks for hydrocarbon reservoirs, second only to gas hydrates [5, 6, 7].

It's worth noting that most evaporite formations comprise only a small percentage of evaporite minerals, and are often interbedded with other sedimentary rocks such as mudstone, marl, and siltstone. One of the most prominent examples of such formations is the Gachsaran Formation, which plays a critical role as a cap rock for hydrocarbon reservoirs in the Middle East, particularly for the Asmari Limestone, a globally significant hydrocarbon reservoir unit [8].

The Gachsaran Formation has been thoroughly studied from various aspects,

encompassing geochemical, mineralogical, and depositional environment [9, 10, 11, 7, 12, 13, 14, 15, 16, 17, 18]. In the Masjed Soleiman oil field, other stratigraphic units that surface include the Mishan, AghaJari, and Bakhtiari Formations (Figure 1). Distinguishing between these formations, particularly the Mishan and Gachsaran Formations, can be challenging due to their similar lithologies in the published 1:100000 geological map [19]; they were not discriminated, and were introduced as "Mishan or Gachsaran" Formation. The main purpose of this study is evaluating ASTER images for mapping the Gachsaran Evaporite Formation and discriminating its lithological units. The results of this study could highlight the effectiveness of using remote sensing for mapping evaporite formations and discriminating their lithological units in new geological maps, as well as for improving available maps.

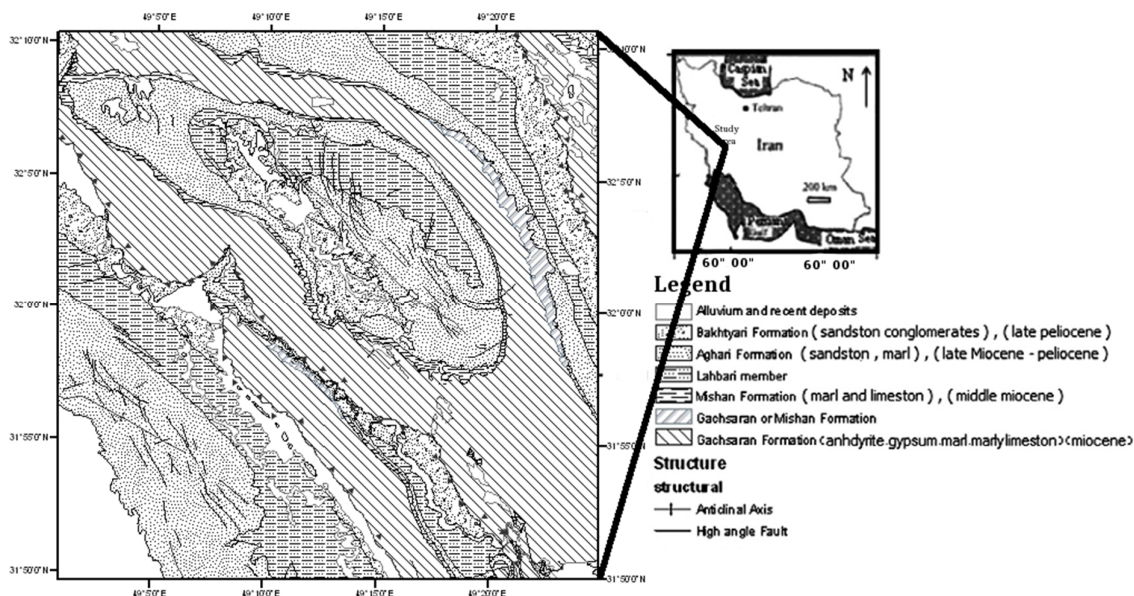


Figure 1. Geological map of Masjed Soleiman oil field area [19].

## 2. Geological Setting

Following the Oligocene period, the Zagros Basin experienced a gradual post-Oligocene regression, leading to the deposition of evaporitic and clastic sediments collectively known as the Fars Group. This group including the Lower Fars, Gachsaran (Miocene), Middle Fars, Mishan (middle

Miocene), and Upper Fars, AghaJari (late Miocene-Pliocene) Formations [20].

The Gachsaran Formation, also recognized by alternative names such as Lower Fars, Evaporate-Chemical Series, and Lower Gypsum Group [21], is notable for its evaporitic nature. The term 'Gach' derives from Persian and refers to gypsum and anhydrite. Evaporate sediments within the

Gachsaran Formation primarily comprise anhydrite, halite, and grey/red marls, with occasional beds of limestone and shale. Halite surface occurrences rarely are reported, and the replacement of anhydrite by gypsum is a characteristic feature [21].

The formation of the evaporate sequence within this formation can be attributed to arid conditions and cycles of transgression-regression in a coastal sabkha-lagoon basin, which was partially proximate to the sea [14]. While the thickness of this sedimentary formation exhibits variation, the complete sequence is estimated to be approximately 1500 meters thick [11].

Following the last major marine deposition period in the Zagros Basin during the late Oligo-Miocene [22], arid conditions and cycles of transgression-regression provided the ideal conditions for the deposition of the Gachsaran Formation within a coastal sabkha-lagoon basin. Two primary facies are recognized within this basin: the central and marginal facies. The central facies is characterized by a higher presence of chemical deposits [10], while the marginal facies includes thicker intervals of limestone and marl, with detrital quartz and feldspar leading to the formation of distinct silty and sandy zones in some areas [12].

One of the main outcrops of the Gachsaran Formation is observed in the Masjed Soleiman oil field. This field is first recognized oil field in the Middle East located between  $31^{\circ} 5' 37''$  N to  $32^{\circ} 10' 46''$  N and  $49^{\circ} 02' 31''$  E to  $49^{\circ} 25' 44''$  E, in the Northern Dezful embayment, which primarily consists of gypsum, anhydrite, and minor beds of red marl. This embayment is part of the south-central region of the Zagros Fold Thrust belt which formed due to the collision of the Arabian Plate and Iranian Block [23, 24]. The active fold thrust belt is divided into the thrust zone, simply folded belt, and coastal plain, with the Dezful embayment serving as a distinct structural unit, bounded by the Mountain Front thrust fault to the northwest, the Kazerun-Borazjan and Izeh transverse faults to the east and southeast, and the Zagros Fore-deep fault to the southwest [11].

Within the studied area, several other stratigraphic units are notable including the Mishan, AghaJari, and Bakhtiari Formations

(Figure 1). The Mishan Formation, which overlies the Gachsaran Formation, exhibits a distinctive composition. Its basal portion comprises limestone and grey marl, followed by alternating layers of grey marl and shelly limestone [10]. The AghaJari Formation consists of brownish to grey calcareous sandstones with veins of gypsum, red marl, and siltstone [25]. The Bakhtiari Formation (late Pliocene - Pleistocene) consists of terrigenous clastic grains in silt to boulder sizes [26].

### 3. Methods and Data

A comprehensive approach combining field observations and ASTER data analysis including the pre-processing of ASTER images, standard Principal Component Analysis (PCA), Directed Principal Component Analysis (DPCA), and band ratio techniques was employed to map the Gachsaran Formation and distinguish its lithological units.

We obtained cloud-free Level 1B ASTER data acquired on April 27, 2001, from the EROS Data Centre. Subsequently, this data was processed using ENVI 4.5 and ArcGIS 9.2. ASTER, a valuable super-spectral imaging system, is situated onboard the Earth Observing System (EOS) TERRA platform, launched on December 18, 1999, into a near-circular, sun-synchronous orbit. The instrument comprises 14 channels, encompassing 3 in the visible-near infrared (VNIR) range (between 0.52 and 0.86  $\mu\text{m}$ ), 6 in the shortwave infrared (SWIR) range (between 1.6 and 2.43  $\mu\text{m}$ ), and 5 in the thermal infrared (TIR) range (between 8.125 and 11.65  $\mu\text{m}$ ), with spatial resolutions of 15, 30, and 90 meters, respectively [27].

#### 3.1. Pre-processing of ASTER imagery

The ASTER LIB product comprises radiance at sensor data that has already been georeferenced to Universal Transverse Mercator (UTM) zone 39 N with the WGS-84 datum. Pre-processing techniques involve essential steps including cross-talk correction of SWIR bands and layer stacking of VNIR and SWIR bands into nine bands with a 15-meter pixel size.

During the acquisition of ASTER data, there's a potential issue known as 'crosstalk,'

where energy from the band 4 detector may leak into adjacent detectors of bands 5 and 9. This phenomenon can result in higher brightness values for bands 5 and 9, leading to anomalous absorption features in bands 6 and 8. These anomalies can, in turn, cause misidentifications of minerals [28].

To address this, pixel radiance at the sensor level was transformed into reflectance at the surface using the Internal Average Relative Reflectance (IARR) method. This algorithm normalizes images based on a scene's average spectrum. Specifically, an average spectrum is computed for the entire scene, and this spectrum is then divided into the spectrum at each pixel within the image [29].

### 3.2. ASTER image processing

We performed a standard principal components transformation on ASTER data using the correlation coefficient matrix. In many cases, multispectral datasets exhibit high levels of correlation between bands. This transformation serves to produce uncorrelated output bands, reducing dimensionality and segregating noise components. It's a linear transformation accomplished by identifying a new set of orthogonal axes [30].

Directed Principal Component Analysis (DPCA), introduced by [31] and further developed by [32], is a method that utilizes subset bands to optimize the identification of specific materials by directing the statistics of the Principal Component (PC). An approach based on the examination of eigenvector loadings in each PC image is used for determining which image contains information related to the spectral signatures of specific target minerals. It is expected that the PC image that collects moderate to high eigenvector loadings for the diagnostic absorptive and reflective bands of the index mineral could be considered as the specific image for that mineral. If the loading of absorptive band is negative in sign, the target area will be enhanced in bright pixels, and if the loading of reflective band is negative, the area will be enhanced in dark pixels.

The core concept of this method revolves around the selection of two reflectance and two absorption bands based on the spectral signature of the target material [33]. The

eigenvector loading plays a crucial role in identifying the appropriate PC for enhancing the desired material. Specifically, a PC with higher eigenvector loadings at reflectance and absorption bands of the target material, but with opposite signs, is sought after. If the PC has high eigenvector loadings with a positive sign for the reflectance band and a high eigenvector loading with a negative sign for the absorption band, the target material appears as bright pixels. Conversely, if the PC has high eigenvector loading with a negative sign for the reflectance band and a high eigenvector loading with a positive sign for the absorption band, it appears as dark pixels.

To select the most appropriate bands for DPCA, the reflectance spectrum of gypsum (obtained from the USGS spectral library) was resampled to match the nine bands of ASTER. Band ratios involve dividing pixel values in one band by values in another band. The absolute radiance values are less critical for target identification since pixel brightness can be influenced by geometric factors such as the angle of illumination and particle size [34]. These factors tend to be approximately constant across all bands. Therefore, dividing the values of the two bands effectively removes these effects, and enhances the spectral differences between materials.

The choice of bands for the ratio image depends on the spectral properties of the target material. Typically, selected bands are those in which the material exhibits both high reflectance and strong absorptive features. The reflective band serves as the numerator, while the absorptive band serves as the denominator. Consequently, the target material appears bright in the resulting ratio image.

### 4. Results

Tables 1 and 2 display the results of applying PCA to the nine reflective bands of ASTER data. Notably, the correlation coefficients between ASTER VNIR and SWIR bands generally exceed 70% (Table 1). The first PC captures approximately 84% of the variance, while the second PC encompasses around 11% of the variances (Table 2). These initial PCs are primarily influenced by topography and the average reflectance of the surface. Consequently,

they are most suitable for general mapping purposes. However, it's worth noting that the subsequent PCs, despite having lower variances in the data, often reveal more subtle spectral differences. The final PC

bands (bands 8 and 9) exhibit a noisy appearance due to their very low variances, accounting for only 0.24%. This noise is typically attributed to the inherent noise in the original data.

**Table 1. Correlation coefficients between VNIR and SWIR bands of ASTER.**

Correlation	Band 1	Band 2	Band 3	Band 4	Band 5	Band 6	Band 7	Band 8	Band 9
Band 1	1.000	0.943	0.8878	0.710	0.635	0.635	0.647	0.668	0.513
Band 2		1.000	0.9593	0.810	0.753	0.755	0.756	0.769	0.645
Band 3			1.000	0.830	0.740	0.746	0.726	0.724	0.651
Band 4				1.000	0.937	0.942	0.909	0.886	0.819
Band 5					1.000	0.987	0.977	0.957	0.880
Band 6						1.000	0.980	0.592	0.886
Band 7							1.000	0.979	0.871
Band 8								1.000	0.839
Band 9									1.000

**Table 2. Eigenvector loadings and variances resulted from applying principal components on 9 ASTER reflective bands.**

Eigenvector	Band 1	Band 2	Band 3	Band 4	Band 5	Band 6	Band 7	Band 8	Band 9	Variance %
PC1	0.338	0.399	0.400	0.349	0.318	0.298	0.333	0.354	0.266	84%
PC2	0.538	0.422	0.422	0.359	-0.113	-0.253	-0.280	-0.269	-0.315	11%
PC3	-0.483	-0.006	-0.006	0.573	0.397	-0.021	-0.276	-0.375	0.247	1.8%
PC4	-0.033	-0.116	-0.116	-0.034	0.4618	0.216	0.160	-0.162	-0.789	1.7%
PC5	0.535	-0.353	-0.353	-0.324	0.502	-0.015	-0.234	-0.250	0.334	0.7%
PC6	0.107	-0.541	-0.541	0.417	0.137	-0.327	0.019	0.562	-0.133	0.35%
PC7	0.253	-0.481	-0.480	0.374	-0.476	0.332	0.165	-0.356	0.039	0.2%
PC8	0.014	0.012	0.012	-0.018	-0.012	-0.755	0.241	-0.154	0.030	0.13%
PC9	-0.0128	0.006	0.006	0.007	0.129	-0.108	0.752	-0.326	0.114	0.1%

The examination of various colour composites of PC images, their visual interpretation, and comparing with the published 1:100000 geological map of the area reveals that the colour composite of PCs 4-5-2 (RGB) is more appropriate to discriminate the Gachsaran Formation from other formations (Figure 2).

Figure 3 shows the reflectance spectra of gypsum (from USGS spectral library) resampled to the nine bands of ASTER. Table 3 indicates eigenvector loadings

resulting from applying DPCA on bands 4, 6, 8, and 9 (these bands were selected due to high reflectance in bands 4 and 8, and low reflectance in bands 6 and 9). Investigation of these eigenvector loading reveals that PC4, which has high eigenvector loading for bands 6 and 8 with opposite signs could enhance gypsum. In this PC, band 6 has a high negative value and band 8 has a high positive value, therefore, gypsum appears as bright pixels (Figure 4).

**Table 3. Eigenvector loading resulted from applying DPCA on bands 4, 6, 8, and 9.**

Eigenvector	Band 4	Band 6	Band 8	Band 9
PC1	0.481	0.516	0.554	0.441
PC2	0.656	0.178	-0.169	-0.713
PC3	0.450	-0.139	-0.694	0.544
PC4	0.367	-0.825	0.427	0.030

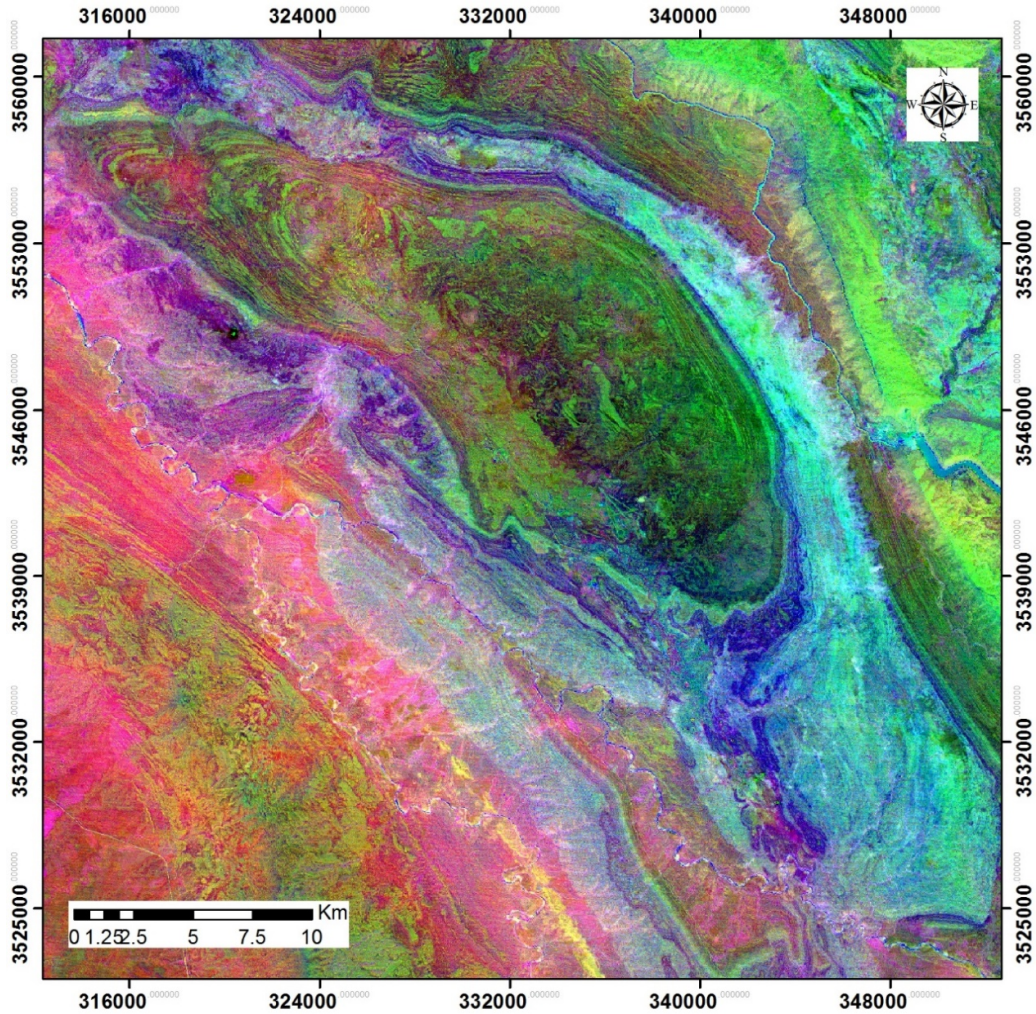


Figure 2. ASTER principal components color composite image as RGB-PC4, PC5, and PC2, overlaid by geological boundaries in black bold lines.

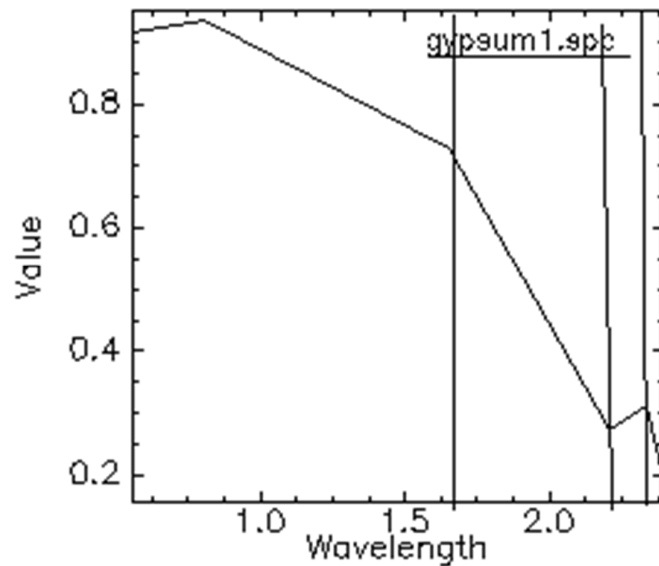
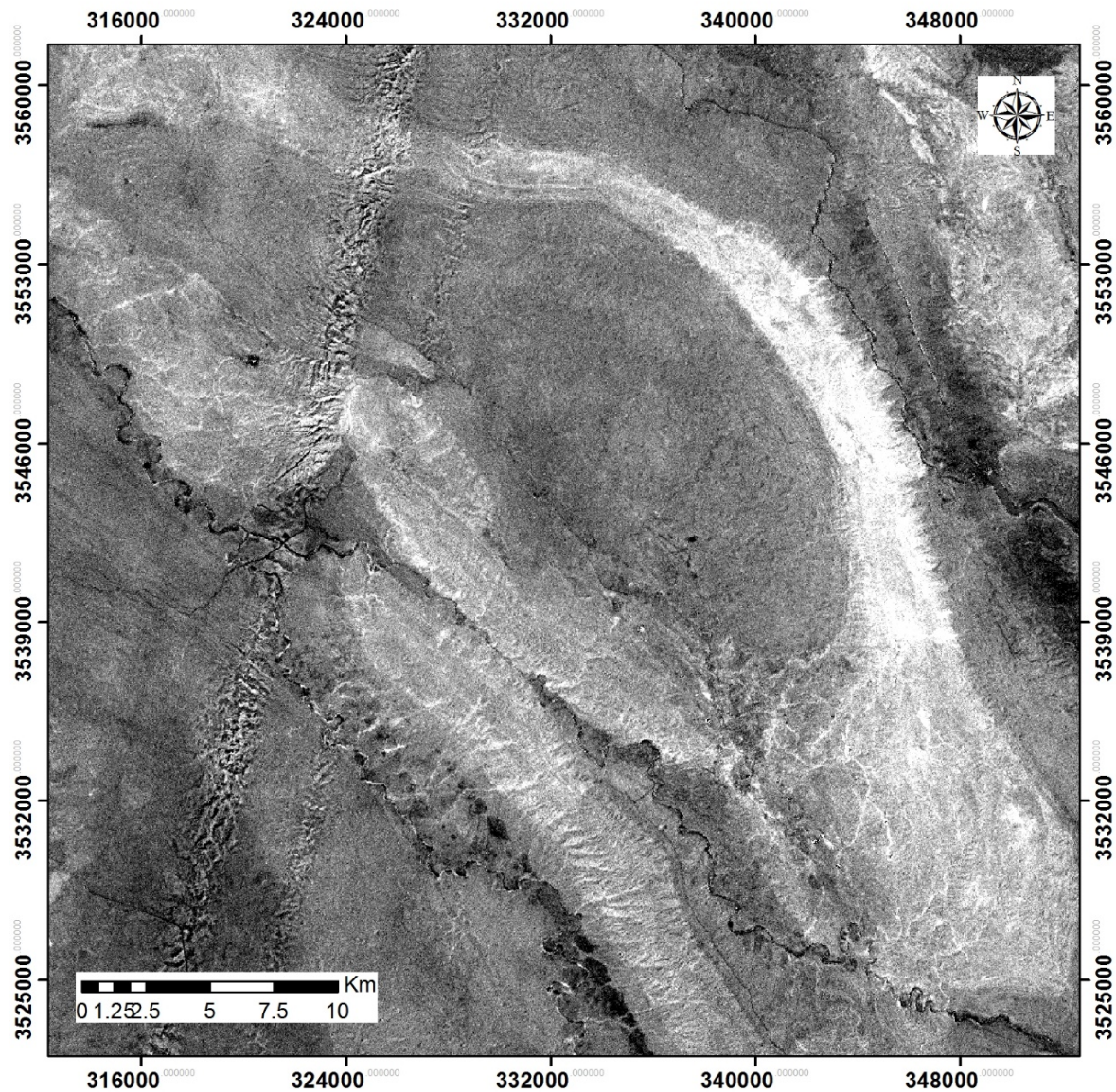


Figure 3. Gypsum spectrum of USGS spectral library resampled to the VNIR-SWIR bands of ASTER.



**Figure 4.** Image of PC4 resulting from applying the DPCA method on bands 4, 6, 8, and 9 overlaid by geological boundaries in black bold lines Brighter pixels in Gachsaran Formation indicate gypsiferous layers.

The results of applying band ratio B2/B1 that has previously been used to discriminate ferric iron [35, 36, 37, 38] is shown in Fig. 5; ferric iron appears as bright pixels in this

figure. Comparing of this figure with the geological map indicates that there are two main ferric iron-rich areas in the Gachsaran Formation.

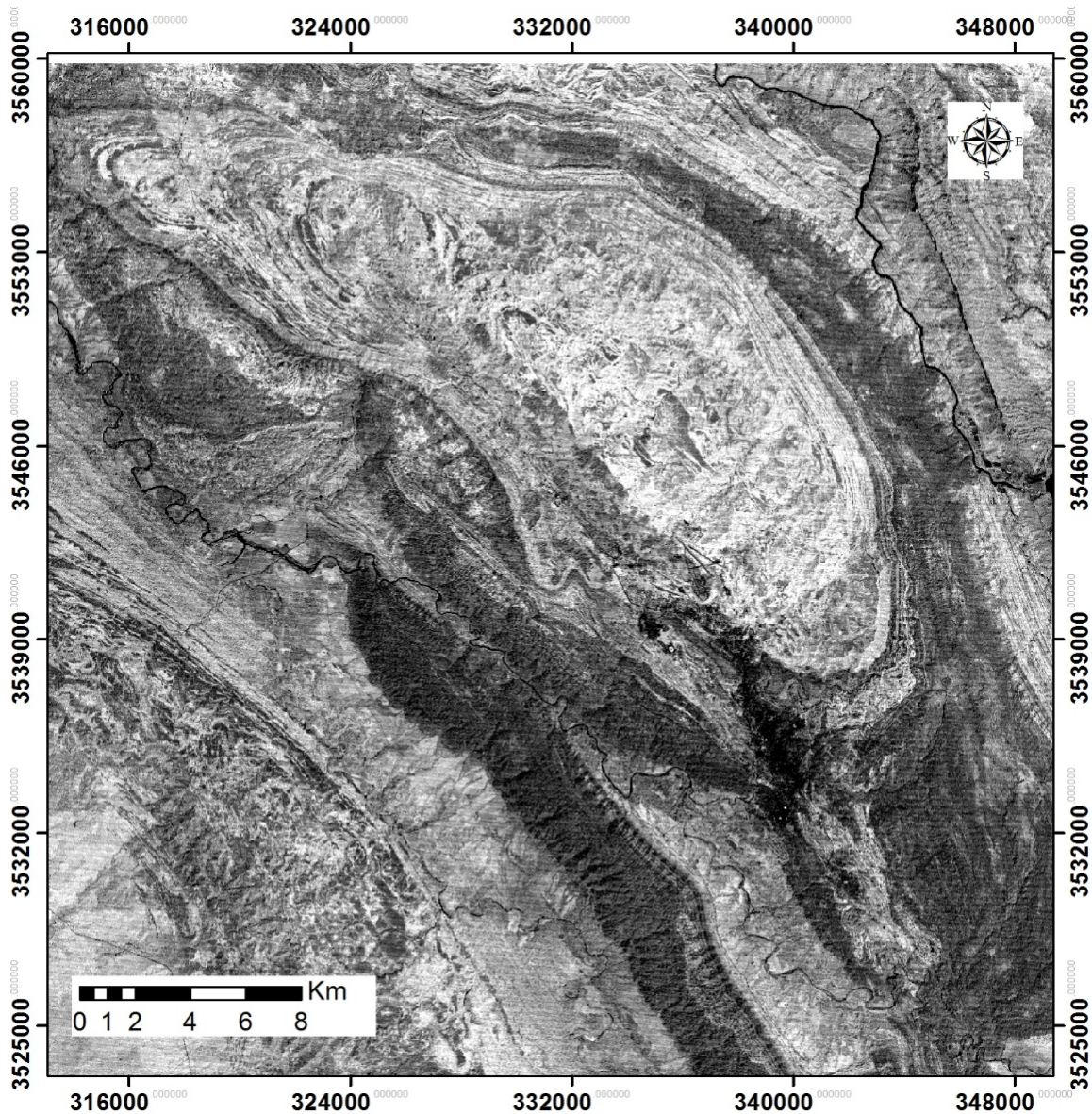


Figure 5. Gray scale image of ASTER band ratio (2/1) overlaid by geological boundaries in black bold lines  
Brighter pixels in Gachsaran Formation indicate ferric iron-bearing red marl.

## 5. Discussion

A colour composite of PCs 4-5-2 (RGB) is more appropriate than other color composite images for discriminating the Gachsaran Formation from other formations (Figure 2). Visual interpretation of this color composite image reveals that the Gachsaran Formation does not appear as a homogenous unit, in contrast to how it is depicted as a homogenous formation in the published geological map [19], where its lithological variations are not shown. The measured radiant flux depends on various

characteristics, with only a minimal variation originating from the spectral reflectance properties of surface material [39]. The PCA method effectively suppresses irradiance effects present in all bands and can identify spectral reflectance features of the ground surface. Principal components produce more colorful composite images compared to spectral color composite images because the data are uncorrelated. These types of composite images have previously been utilized for lithological mapping [40, 41]. Additionally, some areas on this geological

map show challenges in separating the Gachsaran and Mishan Formations (Figure 1); however, visual interpretation of this color composite image suggests that these areas belong to the Gachsaran Formation. A comparison between Fig. 2 and Figs. 5 and 6 indicates a strong agreement between this image and those figures. The brighter pixels in Figs. 5 and 6 correspond to the blue and green pixels in Figure 3, respectively, effectively highlighting the gypsum and red marl outcrops of the Gachsaran Formation.

## 6. Conclusions

Geological maps have traditionally relied on time-consuming and costly field observations during ground surveys, often prone to spatial or thematic inaccuracies. In the recent decades, remote sensing has emerged as a rapid and cost-effective method for acquiring information about outcropping surfaces and enhancing or producing geological maps. In the case of the Masjed Soleiman oil field, ASTER data were utilized to map the Gachsaran Formation and distinguish its lithological units. By employing the PCA method and exploring various color composites of PC images, it was determined that a color composite of PCs 4, 5, and 2 as RGB effectively discriminates the Gachsaran Formation from other formations within the Fars Group.

Furthermore, this particular color composite provides clear differentiation between the Mishan and Gachsaran Formations, even in areas where the published geological map lumps them together as 'Mishan or Gachsaran Formation.' The application of DPCA to bands 4, 6, 8, and 9 resulted in the successful mapping of gypsiferous outcrops within the PC4. Additionally, the use of band ratio 2/1 enhanced the response of ferric iron, corresponding to the red marls of this formation.

Collectively, the results obtained through PCA, DPCA, and band ratios not only effectively discriminated the Gachsaran Formation from other sedimentary formations but also enhanced the recognition of its lithological variations. This study underscores the potential of ASTER data processing, combined with limited fieldwork, as a time- and cost-efficient approach for

mapping evaporite formations and distinguishing their lithological variations. Such methodologies hold promise for generating new geological maps or refining existing ones, particularly in arid and semi-arid regions.

## Acknowledgments

We are grateful to anonymous reviewer for helpful and valuable review of the manuscript. Also we would like to thank Hassan Amiri Bakhtiari, of National Iranian South Oil Company (NISOC) for providing logistics during field works and Noel White, University of Tasmania, Australia, for reviewing the earlier version of the manuscript. Support of the Research Council of Shiraz University is gratefully acknowledged.

## References

- [1]. Watts, D. R., & Harris, N. B. (2005). Mapping granite and gneiss in domes along the North Himalayan antiform with ASTER SWIR band ratios. *Geological Society of America Bulletin*, 117(7-8), 879-886.
- [2]. Qiu, F., Abdelsalam, M., & Thakkar, P. (2006). Spectral analysis of ASTER data covering part of the Neoproterozoic Allaqi-Heiani suture, Southern Egypt. *Journal of African Earth Sciences*, 44(2), 169-180.
- [3]. Gad, S., & Kusky, T. (2007). ASTER spectral ratioing for lithological mapping in the Arabian-Nubian shield, the Neoproterozoic Wadi Kid area, Sinai, Egypt. *Gondwana research*, 11(3), 326-335.
- [4]. Afzal, P., Abdideh, M., & Daneshvar Saein, L. (2023). Separation of productivity index zones using fractal models to identify promising areas of fractured reservoir rocks. *Journal of Petroleum Exploration and Production Technology*, 1-10.
- [5]. Melvin, J. L. (Ed.). (1991). *Evaporites, petroleum and mineral resources*.
- [6]. Kendall, A. C. (1983). Unconformity-associated replacement limestones after anhydrite in Mississippian of Williston Basin. *AAPG Bulletin*, 67(3), 494-495.
- [7]. Warren, J. K., & Warren, J. K. (2016). Hydrocarbons and evaporites. *Evaporites: A Geological Compendium*, 959-1079.
- [8]. Bahroudi, A., & Koyi, H. A. (2004). Tectono-sedimentary framework of the Gachsaran Formation in the Zagros foreland

- basin. *Marine and Petroleum Geology*, 21(10), 1295-1310.
- [9]. O'Brien, C. A. E. (1950). Tectonic problems of the oilfield belt of southwest Iran. In *Proceedings of the 18th International Geological Congress, Great Britain, pt* (Vol. 6, pp. 45-58).
- [10]. Falcon, N. L. (1958). Position of Oil Fields of Southwest Iran with Respect to Relevant Sedimentary Basins: Middle East.
- [11]. James, G. A., & Wynd, J. G. (1965). Stratigraphic nomenclature of Iranian oil consortium agreement area. *AAPG bulletin*, 49(12), 2182-2245.
- [12]. Gill, W. D., & Ala, M. A. (1972). Sedimentology of Gachsaran Formation (Lower Fars Series), Southwest Iran. *AAPG Bulletin*, 56(10), 1965-1974.
- [13]. Safari, H. O., Pirasteh, S., Pradhan, B., & Gharibvand, L. K. (2010). Use of remote sensing data and GIS tools for seismic hazard assessment for shallow oilfields and its impact on the settlements at Masjed-i-Soleiman Area, Zagros Mountains, Iran. *Remote Sensing*, 2(5), 1364-1377.
- [14]. Bahadori, A., Carranza, E. J. M., & Soleimani, B. (2011). Geochemical analysis of evaporite sedimentation in the Gachsaran Formation, Zeloi oil field, southwest Iran. *Journal of Geochemical Exploration*, 111(3), 97-112.
- [15]. Tangestani, M. H., & Validabadi, K. (2014). Mineralogy and geochemistry of alteration induced by hydrocarbon seepage in an evaporite formation; a case study from the Zagros Fold Belt, SW Iran. *Applied geochemistry*, 41, 189-195.
- [16]. Perry, J.T., Setudehnia, A., 1966, Geological compilation map 1:100,000 drawing No. 25474 w.
- [17]. Nabilou, M., Afzal, P., Arian, M., Adib, A., Kheyrollahi, H., Foudazi, M., & Ansarirad, P. (2022). The relationship between Fe mineralization and magnetic basement faults using multifractal modeling in the Esfordi and Behabad Areas (BMD), Central Iran. *Acta Geologica Sinica-English Edition*, 96(2), 591-606..
- [18]. Saed, S., Azizi, H., Daneshvar, N., Afzal, P., Whattam, S. A., & Mohammad, Y. O. (2022). Hydrothermal alteration mapping using ASTER data, Takab-Baneh area, NW Iran: A key for further exploration of polymetal deposits. *Geocarto International*, 37(26), 11456-11482.
- [19]. BEHBAHANI, B., HARATI, H., AFZAL, P., & LOTFI, M. (2023). Determination of alteration zones applying fractal modeling and Spectral Feature Fitting (SFF) method in Saryazd porphyry copper system, central Iran. *Bulletin of the Mineral Research and Exploration*, (early view), 1-1.
- [20]. Stöcklin, J. (1968). Structural history and tectonics of Iran: a review. *AAPG bulletin*, 52(7), 1229-1258.
- [21]. Berberian, M., & King, G. C. P. (1981). Towards a paleogeography and tectonic evolution of Iran. *Canadian journal of earth sciences*, 18(2), 210-265.
- [22]. National Iranian Oil Company (NIOC), 1995. The condition of existence hydrocarbon seepage in Masjed Soleiman City, Internal Report, NIOC. Tehran, Iran.
- [23]. Motiei H (1973). Geology of Iran, Stratigraphy of Zagros. Geology Organization of Iran, Tehran.
- [24]. Nairn, A. E. M., & Alsharhan, A. S. (1997). *Sedimentary basins and petroleum geology of the Middle East*. Elsevier.
- [25]. Yamaguchi, Y., Kahle, A. B., Tsu, H., Kawakami, T., & Pniel, M. (1998). Overview of advanced spaceborne thermal emission and reflection radiometer (ASTER). *IEEE Transactions on geoscience and remote sensing*, 36(4), 1062-1071.
- [26]. Mars, J. C., & Rowan, L. C. (2006). Regional mapping of phyllic-and argillic-altered rocks in the Zagros magmatic arc, Iran, using Advanced Spaceborne Thermal Emission and Reflection Radiometer (ASTER) data and logical operator algorithms. *Geosphere*, 2(3), 161-186.
- [27]. Kruse, F. A. (1988). Use of airborne imaging spectrometer data to map minerals associated with hydrothermally altered rocks in the northern grapevine mountains, Nevada, and California. *Remote Sensing of Environment*, 24(1), 31-51.
- [28]. Cole, M. (1987). Remote Sensing: Principles and Interpretation.
- [29]. Crosta, A. P. (1989). Enhancement of Landsat Thematic Mapper imagery for residual soil mapping in SW Minas Gerais State Brazil, a prospecting case history in greenstone belt terrain. In *Proceedings of the 7<sup>th</sup> ERIM Thematic Conference on Remote Sensing for Exploration Geology, 1989*.
- [30]. Loughlin, W. P. (1991). Principal component analysis for alteration

mapping. *Photogrammetric Engineering and Remote Sensing*, 57(9), 1163-1169.

[31]. Crosta, A. P., De Souza Filho, C. R., Azevedo, F., & Brodie, C. (2003). Targeting key alteration minerals in epithermal deposits in Patagonia, Argentina, using ASTER imagery and principal component analysis. *International journal of Remote sensing*, 24(21), 4233-4240.

[32]. Adams, J. B., & Gillespie, A. R. (2018). *Remote sensing of landscapes with spectral images: A physical modeling approach*. Cambridge University Press.

[33]. Almeida-Filho, R., Miranda, F. P., & Yamakawa, T. (1999). Remote detection of a tonal anomaly in an area of hydrocarbon microseepage, Tucano basin, north-eastern Brazil. *International Journal of Remote Sensing*, 20(13), 2683-2688.

[34]. Wang, Y., & Ding, X. (2000). Hydrocarbon alteration characteristics of soils and mechanism for detection by remote sensing in east Sichuan area, China. *Natural Resources Research*, 9(4), 295-305.

[35]. Ma, Y., Liu, C., Zhao, J., Huang, L., Yu, L., & Wang, J. (2007). Characteristics of bleaching of sandstone in northeast of Ordos Basin and its relationship with natural gas leakage. *Science in China Series D: Earth Sciences*, 50(Suppl 2), 153-164.

[36]. Sadeghi, B., Khalajmasoumi, M., Afzal, P., Moarefvand, P., Yasrebi, A. B., Wetherelt, A., ... & Ziazarifi, A. (2013). Using ETM+ and ASTER sensors to identify iron occurrences in the Esfordi 1: 100,000 mapping sheet of Central Iran. *Journal of African Earth Sciences*, 85, 103-114.

[37]. Sabine, C. (1999). Remote sensing strategies for mineral exploration. *Remote Sensing for the Earth Sciences—Manual of Remote Sensing*, 375-447.

[38]. Gomez, C., Delacourt, C., Allemand, P., Ledru, P., & Wackerle, R. (2005). Using ASTER remote sensing data set for geological mapping, in Namibia. *Physics and Chemistry of the Earth, Parts A/B/C*, 30(1-3), 97-108.

[39]. Amer, R., Kusky, T., & Ghulam, A. (2010). Lithological mapping in the Central Eastern Desert of Egypt using ASTER data. *Journal of African Earth Sciences*, 56(2-3), 75-82.

[40]. Ghrefat, H., Kahal, A. Y., Abdelrahman, K., Alfaifi, H. J., & Qaysi, S. (2021). Utilization of multispectral landsat-8 remote sensing data for lithological mapping of southwestern Saudi Arabia. *Journal of King Saud University-Science*, 33(4), 101414.

[41]. Aboelkhair, H., Abdelhalim, A., Hamimi, Z., & Al-Gabali, M. (2020). Reliability of using ASTER data in lithologic mapping and alteration mineral detection of the basement complex of West Berenice, Southeastern Desert, Egypt. *Arabian Journal of Geosciences*, 13, 1-20.

## نقشه برداری واحدهای سنگ شناسی یک سازند تبخیری با استفاده از داده‌های سنجنده استر، مطالعه موردی زاگرس چین خورده، جنوب غرب ایران

خدیدجه ولیدآبادی بزچلوئی\*، مجید هاشمی تنگستانی

بخش علوم زمین، دانشگاه شیراز ایران

ارسال ۲۰۲۳/۰۹/۲۰، پذیرش ۲۰۲۳/۱۱/۱۲

\* نویسنده مسئول مکاتبات: khvalid@gmail.com

### چکیده:

تبخیرها رسوباتی هستند که در اثر تبخیر یک محلول آبی به صورت شیمیایی رسوب می‌کنند. بیشتر سازندهای تبخیری، علاوه بر کانی‌های تبخیری، شامل سنگ‌های آواری مانند گل سنگ، مارن و سیلت استون می‌باشند. روش‌های آنالیز مؤلفه اصلی (PCA)، آنالیز مؤلفه اصلی هدایت‌شده (DPCA) و نسبت باند، بر روی داده‌های سنجنده ASTER برای نقشه‌برداری سازند تبخیری گچساران و تشخیص واحدهای سنگ‌شناسی آن در میدان نفتی واقع در جنوب غرب ایران استفاده شد. این میدان اولین میدان نفتی شناخته شده در خاورمیانه است. ترکیب رنگی مؤلفه‌های ۴، ۵، و ۲، به صورت تصویر RGB، به طور مؤثر این سازند را از دیگر سازندهای رسوبی متمایز کرد. طیف گچ بازنویسی شده به مرکز باند سنجنده ASTER، بازتاب در باندهای ۴ و ۸ و جذب در باندهای ۶ و ۹ را نشان داد. در نتیجه، این باندها برای اجرای روش DPCA انتخاب شدند. PC4 رخنمون‌های گچی را به صورت پیکسل‌های روشن متمایز نمود، در حالی که نسبت باندی ۱/۲ بخوبی واحدهای آهن دار را به صورت پیکسل‌های روشن بارزسازی نمود. نتایج این مطالعه نشان می‌دهد که پردازش تصویر ASTER یک روش مقرون به صرفه است که می‌تواند برای نقشه برداری سازندهای تبخیری و تشخیص واحدهای سنگ شناسی آنها استفاده شود.

کلمات کلیدی: استر، واحد تبخیری، تحلیل مولفه اصلی، نسبت باندی